nature medicine

FOCUS | LETTERS

https://doi.org/10.1038/s41591-019-0357-y

A single dose of neoadjuvant PD-1 blockade predicts clinical outcomes in resectable melanoma

Alexander C. Huang[1,2,3,4,16*], Robert J. Orlowski[1,11,16], Xiaowei Xu[4,5], Rosemarie Mick[3,4,6], Sangeeth M. George[7,12], Patrick K. Yan[2,7], Sasikanth Manne[2,7], Adam A. Kraya[1,4], Bradley Wubbenhorst[1,4], Liza Dorfman[1,4], Kurt D'Andrea[1,4], Brandon M. Wenz[1,4], Shujing Liu[4,5], Lakshmi Chilukuri[2,7], Andrew Kozlov[4,8], Mary Carberry[1,4], Lydia Giles[1,4], Melanie W. Kier[1], Felix Quagliarello[2,13], Suzanne McGettigan[1,4], Kristin Kreider[1,4], Lakshmanan Annamalai[9], Qing Zhao[9], Robin Mogg[9,14], Wei Xu[1,4], Wendy M. Blumenschein[9], Jennifer H. Yearley[9], Gerald P. Linette[1,2,3,4], Ravi K. Amaravadi[1,4], Lynn M. Schuchter[1,4], Ramin S. Herati[1,2], Bertram Bengsch[2,15], Katherine L. Nathanson[1,3,4], Michael D. Farwell[4,8,17], Giorgos C. Karakousis[4,10,17], E. John Wherry[2,3,4,7,17*] and Tara C. Mitchell[1,4,17*]

Immunologic responses to anti-PD-1 therapy in melanoma patients occur rapidly with pharmacodynamic T cell responses detectable in blood by 3 weeks. It is unclear, however, whether these early blood-based observations translate to the tumor microenvironment. We conducted a study of neoadjuvant/adjuvant anti-PD-1 therapy in stage III/IV melanoma. We hypothesized that immune reinvigoration in the tumor would be detectable at 3 weeks and that this response would correlate with disease-free survival. We identified a rapid and potent anti-tumor response, with 8 of 27 patients experiencing a complete or major pathological response after a single dose of anti-PD-1, all of whom remain disease free. These rapid pathologic and clinical responses were associated with accumulation of exhausted CD8 T cells in the tumor at 3 weeks, with reinvigoration in the blood observed as early as 1 week. Transcriptional analysis demonstrated a pretreatment immune signature (neoadjuvant response signature) that was associated with clinical benefit. In contrast, patients with disease recurrence displayed mechanisms of resistance including immune suppression, mutational escape, and/or tumor evolution. Neoadjuvant anti-PD-1 treatment is effective in high-risk resectable stage III/IV melanoma. Pathological response and immunological analyses after a single neoadjuvant dose can be used to predict clinical outcome and to dissect underlying mechanisms in checkpoint blockade.

Clinical responses to anti-PD-1 therapies can occur rapidly[1,2]. A pharmacodynamic response including reinvigoration of exhausted-phenotype CD8 T cells (T_{EX}) can be detected in blood of cancer patients after a single dose[3,4]. However, the precise type(s) of T cells in the tumor that respond to anti-PD-1 remains poorly understood. Moreover, whereas early immunological responses to checkpoint blockade are observed at 3 weeks in blood, the kinetics of immune reinvigoration in the tumor and the relationship to pathological response and clinical outcomes are unclear.

We conducted a neoadjuvant/adjuvant anti-PD-1 clinical trial in stage III/IV resectable melanoma. This approach provided early on-treatment tumor tissue at resection and insights into the mechanisms of PD-1 blockade. Our study demonstrated the clinical feasibility of neoadjuvant/adjuvant anti-PD-1 therapy in melanoma, and identified a rapid pathological and immunologic response in tumors. Complete pathological responses could be identified by 3 weeks and correlated with disease-free survival (DFS). Data from early on-treatment resected tumor indicate that T_{EX}, but not bystander cells, are a major responding cell type. Studies in an additional cohort identified reinvigoration of T_{EX} as early as day 7 after the first dose of anti-PD-1. Finally, in patients who developed disease recurrence, potential mechanisms of resistance were identified.

Results

A pharmacodynamic immune response can be detected in blood 3 weeks after initiation of PD-1 blockade[3,4]. To understand the

[1]Department of Medicine, Perelman School of Medicine, University of Pennsylvania, Philadelphia, PA, USA. [2]Institute for Immunology, Perelman School of Medicine, University of Pennsylvania, Philadelphia, PA, USA. [3]Parker Institute for Cancer Immunotherapy at University of Pennsylvania, Philadelphia, PA, USA. [4]Abramson Cancer Center, Perelman School of Medicine, University of Pennsylvania, Philadelphia, PA, USA. [5]Department of Pathology and Laboratory Medicine, Perelman School of Medicine, University of Pennsylvania, Philadelphia, PA, USA. [6]Department of Biostatistics, Epidemiology and Informatics, Perelman School of Medicine, University of Pennsylvania, Philadelphia, PA, USA. [7]Department of Systems Pharmacology and Translational Therapeutics, Perelman School of Medicine, University of Pennsylvania, Philadelphia, PA, USA. [8]Department of Radiology, Perelman School of Medicine, University of Pennsylvania, Philadelphia, PA, USA. [9]Merck Research Laboratories, Kenilworth, NJ, USA. [10]Department of Surgery, Perelman School of Medicine, University of Pennsylvania, Philadelphia, PA, USA. [11]Present address: Merck & Co., Inc., Kenilworth, NJ, USA. [12]Present address: Bristol-Myers Squibb, Lawrenceville, NJ, USA. [13]Present address: Stem Cell Technologies, Vancouver, British Columbia, Canada. [14]Present address: Bill & Melinda Gates Medical Research Institute, Cambridge, MA, USA. [15]Present address: Department of Medicine II, Gastroenterology, Hepatology, Endocrinology, and Infectious Diseases, University Medical Center Freiburg, Freiburg, Germany. [16]These authors contributed equally: A. C. Huang, R. J. Orlowski. [17]These authors jointly supervised this work: M. D. Farwell, G. C. Karakousis, E. J. Wherry, T. C. Mitchell. *e-mail: alexander.huang@uphs.upenn.edu; wherry@pennmedicine.upenn.edu; tara.mitchell@uphs.upenn.edu

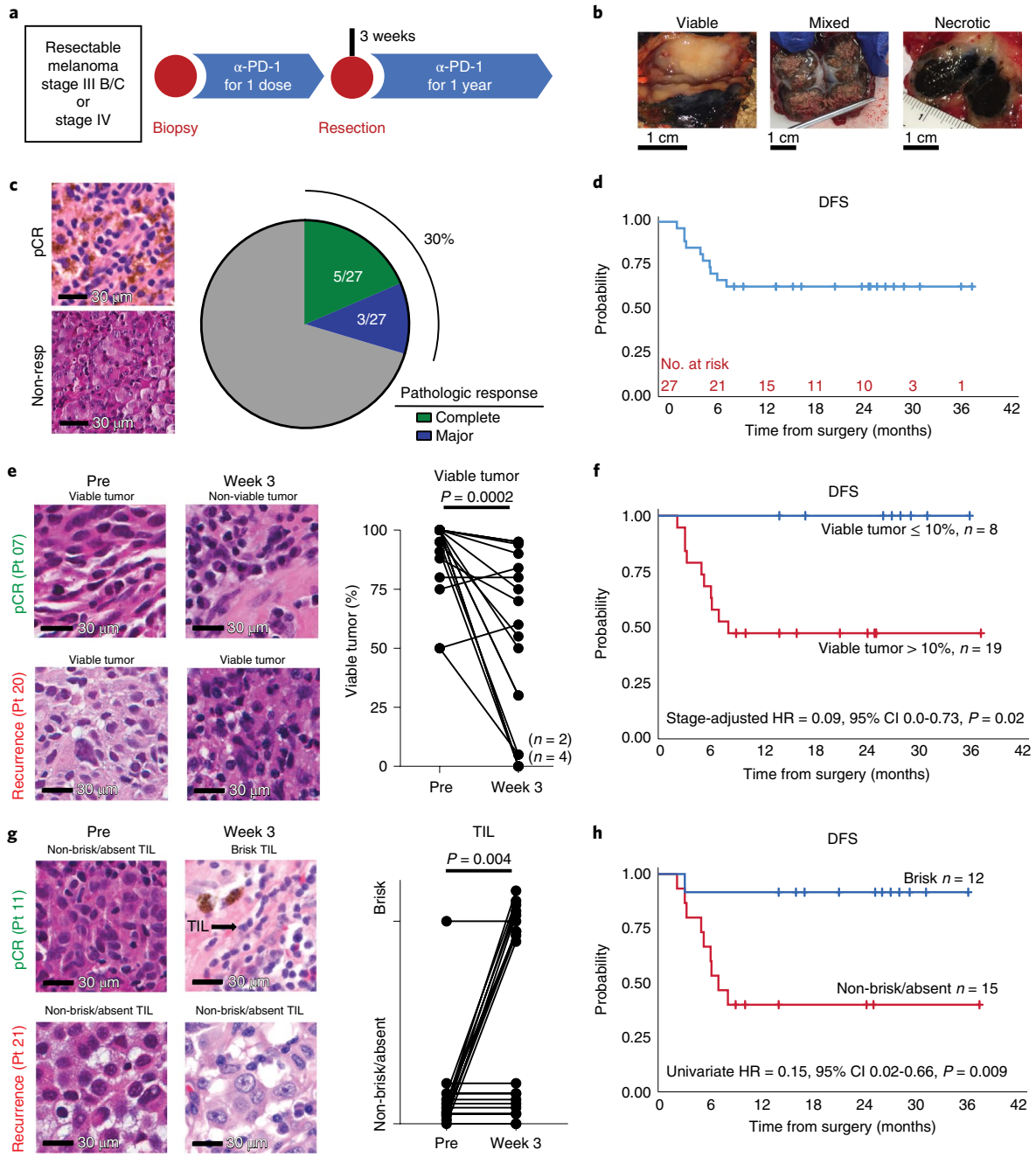

Fig. 1 | Pathologic response and TILs are predictive of clinical outcome after a single dose of anti-PD-1. a, Schema of the neoadjuvant and then adjuvant pembrolizumab clinical trial. **b**, Representative images of viable, mixed, and necrotic tumors resected at the 3-week post-treatment time point. **c**, Representative H&E images of pCR and non-response (non-resp) (left) and fraction of patients with complete pathologic response and major pathologic response (right). **d**, Kaplan–Meier estimate of DFS. **e**, Representative H&E images (left) and changes in the percentage of viable tumor in pre-treatment and post-treatment tumors (right, $n = 20$); P value calculated using two-sided Wilcoxon matched-pairs test. **f**, Kaplan–Maier estimate of DFS stratified according to pathologic response. Cox proportional hazards regression modeling was used to calculate hazard ratio. **g**, Changes in TIL infiltration in pre-treatment and post-treatment tumors ($n = 20$); P value calculated using McNemar's test. **h**, Kaplan–Maier estimate of DFS stratified according to TIL response. Cox proportional hazards regression modeling was used to calculate hazard ratio. 95% CI, 95% confidence interval; HR, hazard ratio; Pt, patient.

early effects of anti-PD-1 in tumors, we conducted an investigator-initiated clinical trial of neoadjuvant anti-PD-1 (pembrolizumab) in stage IIIB/C or IV melanoma. All patients underwent baseline pretreatment biopsy and received a single dose of pembrolizumab (200 mg), followed by complete resection 3 weeks later and adjuvant therapy (Fig. 1a). Twenty-nine patients were enrolled and treated (Supplementary Table 1). Patients proceeded to surgical resection at 3 weeks (median 21 days, range 17–42). Median interval between surgery and initiation of adjuvant pembrolizumab was 23 days (range 13–39). There were no unexpected adverse events (Supplementary Table 2); the rate of grade 3 or higher adverse events not attributed to pembrolizumab or to surgery alone was not higher than 30%, the prespecified safety end point (observed rate was 0%, $P = 0.0002$, z test). There were no unexpected delays in surgery or adjuvant pembrolizumab, or unexpected surgical complications.

We assessed the pathologic response after 1 dose of pembrolizumab in the resection specimens of 27 patients available at time of data cut-off. Resected tumor had features of completely viable, mixed viable and necrotic, or completely necrotic tumor on gross examination (Fig. 1b). On histologic assessment, 8 of 27 patients (29.6%; 95% confidence interval, 13.8–50.2%) had a complete (no residual tumor identified; $n=5$) or major (10% or less viable tumor cells; $n=3$) pathologic response[5,6] (Fig. 1c). The median duration of follow-up for DFS was 25 months; median DFS has not been reached. The 1-year DFS rate ± s.e.m. was 63% ± 9% (Fig. 1d).

Approximately 30% of patients had a complete or major pathologic response after 1 dose of pembrolizumab, consistent with a recent neoadjuvant anti-PD-1 clinical trial in melanoma that observed a pathologic complete response (pCR) of 25% after 4 doses of nivolumab[7]. In 20 patients with paired pre- and post-treatment tumor samples, the percentage of viable tumor significantly decreased after treatment (Fig. 1e). All patients with complete or major pathologic responses remain disease free (Fig. 1f); viable tumor ≤10% at resection was associated with a low risk of recurrence independent of stage (Supplementary Table 3). Lactate dehydrogenase, BRAF status, and tumor burden (unidimensional tumor diameter) were not associated with recurrence (Supplementary Table 3). In 20 patients with paired samples, a single dose of pembrolizumab significantly increased the fraction of patients with brisk tumor infiltrating lymphocytes (TILs) (Supplementary Table 4 and Fig. 1g) which was also associated with complete or major pathologic response (Supplementary Table 5 and Extended Data Fig. 1) and significantly improved DFS (Supplementary Table 3 and Fig. 1h).

We examined a subset of 6 patients that had early imaging at 3 weeks (trial no. UPCC11615). ^{18}F-fluorodeoxyglucose (FDG) positron emission tomography–computed tomography (PET-CT) scans were performed at baseline and before surgical resection; images were analyzed per RECIST 1.1. Consistent with the pathological responses, radiographic responses were observed after one dose of anti-PD-1. In 3 patients, we observed a ≥20% decrease in tumor diameter and these patients remained recurrence free (Fig. 2a). In contrast, the 3 patients without evidence of tumor shrinkage at 3 weeks had recurrences. Changes in tumor size at 3 weeks correlated with the percentage of viable tumor observed histologically (Fig. 2b,c). However, changes in FDG avidity were not associated with response (data not shown). The percentage of viable tumor at 3 weeks was correlated with a change in tumor dimensions by imaging and recurrence status which were both inversely correlated with TIL infiltration (Fig. 2d,e and Supplementary Table 5).

Given the rapid pathological effects of anti-PD-1, we hypothesized that the reinvigoration of anti-tumor immune responses might occur before 3 weeks. Indeed, there is anecdotal evidence of expansion of CD39$^+$ T_{EX} 9 days after anti-PD-1[8]. We conducted an additional trial of anti-PD-1 (UPCC02616) with blood collected at day 7 after initiation of therapy. We observed robust increases in Ki67$^+$ CD8 T cells at day 7; the responding cells were PD-1$^+$ and enriched for cells that coexpressed PD-1 and CTLA-4 (Fig. 2f,g). This response peaked at day 7 and then declined. Analysis of the Ki67$^+$ cells at day 7 and week 3 showed similarity in expression of markers of differentiation state (CD45RA, CD27), inhibitory receptors (PD-1, CTLA-4), and other markers of T cell exhaustion (CD39) (Fig. 2h,i), indicating similar qualitative responses at day 7 and 3 weeks. Ki67$^+$ cells pretreatment also had similar phenotype, suggesting that PD-1 blockade reinvigorates a pre-existing pool of T_{EX}(Fig. 2i). The robust response of T_{EX}-like CD8 T cells to anti-PD-1 as early as 7 days post-treatment is consistent with the robust tumor eradication in many patients by 3 weeks.

To further investigate the nature of the rapid intratumoral response to anti-PD-1, we compared peripheral blood mononuclear cells (PBMCs) to TILs at week 3. Increased proliferation of CD8, CD4, and FoxP3$^+$ regulatory T cells (Tregs) was detected in the blood after anti-PD-1 (Extended Data Fig. 2a), as described[3]. In the tumor, CD8 T cell proliferation increased (Extended Data Fig. 2b) and, as expected[9,10], pembrolizumab treatment increased CD8 T cell infiltration (Fig. 3a). The majority of CD8 T cells in the tumor were CD45RA^{lo}CD27^{hi}. PD-1 was coexpressed with Tim-3, CTLA-4, LAG3, TIGIT, and CD39 (ref. [11]), and many of these TIL CD8 T cells expressed high Eomes, but low T-bet (Fig. 3b,c), consistent with the phenotype of T_{EX}[12,13]. In addition, the majority of CD8 T cells in the tumor were bound by pembrolizumab (Fig. 3d).

At 3 weeks there was a robust increase in Ki67 in PD-1$^+$ and PD-1$^+$CTLA-4$^+$ CD8 T cells in the blood. Although there was an increase in Ki67 in PD-1$^+$ CD8 T cells in the tumor, the PD-1$^+$CTLA-4$^+$ subset lacked a consistent increase in Ki67, whereas the proportion of PD-1$^+$CTLA-4$^+$ CD8 T cells in the tumor increased following treatment (Fig. 3e). This finding suggested that: (1) immune reinvigoration in the tumor may be early and transient, while systemic reinvigoration may be sustained, and/or (2) T cells may be reinvigorated in the periphery before trafficking to the tumor.

We observed a high frequency of PD-1$^+$CD39$^+$ CD8 T cells in the TILs pretreatment (Fig. 3b), consistent with tumor-reactive T cells[8]. To examine tumor specificity in more detail, we examined gp100 and cytomegalovirus (CMV)-specific CD8 T cells using HLA/peptide tetramers pre- and post-treatment in two patients. There were no consistent changes for these populations in the blood following treatment. However, in both patients, gp100-specific CD8 T cells were present at higher frequencies in the tumor than blood pretreatment and these cells increased in frequency after anti-PD-1 (Fig. 3f). Conversely, CMV-specific CD8 T cells in the tumor did not expand after treatment. At week 3, gp100-specific CD8 T cells in the tumor were CD45RA^{lo}CD27^{hi}; expressed high PD-1, Tim-3, and CTLA-4; and most were Eomes^{hi}T-bet^{lo} (Fig. 3g,h). Compared with blood, the gp100-specific CD8 T cells in the tumor had similar PD-1, more Tim-3 and CTLA-4, but less Ki67. In contrast, CMV-specific CD8 T cells in the blood were CD45RA^{hi}CD27^{lo}, coexpressed Eomes and T-bet, and had lower inhibitor receptors (Fig. 3h). Thus, melanoma-specific CD8 T cells in the blood and tumor of a subset of patients had a phenotype consistent with T_{EX} in the tumor and increased numerically after anti-PD-1.

We next studied the cellular determinants of anti-PD-1 response versus resistance in this cohort. Anti-PD-1 increased CD8 T cells in the tumor (Fig. 3a), but also increased PD-L1 and Tregs (Extended Data Fig. 3a and Fig. 4a). Proliferation of CD8 T cells in the tumor also correlated with Treg proliferation (Extended Data Fig. 3b), suggesting rapid upregulation of immunoregulatory feedback mechanisms. Random forest analysis in the tumor post-treatment revealed Eomes expression and Treg proliferation as strong correlates of recurrence-free survival (Extended Data Fig. 3c). A high percentage of Eomes^{hi}T-bet^{lo} T_{EX} was associated with clinical benefit and Treg proliferation was associated with recurrence and poor DFS (Extended Data Fig. 3d and Fig. 4b). Treg proliferation was inversely correlated with the frequency of Eomes^{hi}T-bet^{lo} T_{EX} (Extended Data Fig. 3e). Random forest analysis of pretreatment immune parameters identified baseline Ki67 expression by non-naïve CD8 T cells as associated with clinical benefit (Fig. 4c and Extended Data Fig. 3f–h), suggesting that pre-existing CD8 T cell responses drive clinical responses to anti-PD-1 (refs. [10,14]).

NanoString analysis of post-treatment tumor revealed a distinct signature of T cell activation compared with pretreatment including *CD8A, CD8B, GZMA, GZMK, ZAP70, LAT*, and *CD69* (Extended Data Fig. 4a). Pretreatment, we also identified a strong neoadjuvant response signature (NRS) including genes involved in T cell activation, adaptive immune response, and T cell migration (Fig. 4d–f) that correlated with post-treatment TIL responses and recurrence-free survival. This finding is consistent with T cell-inflamed

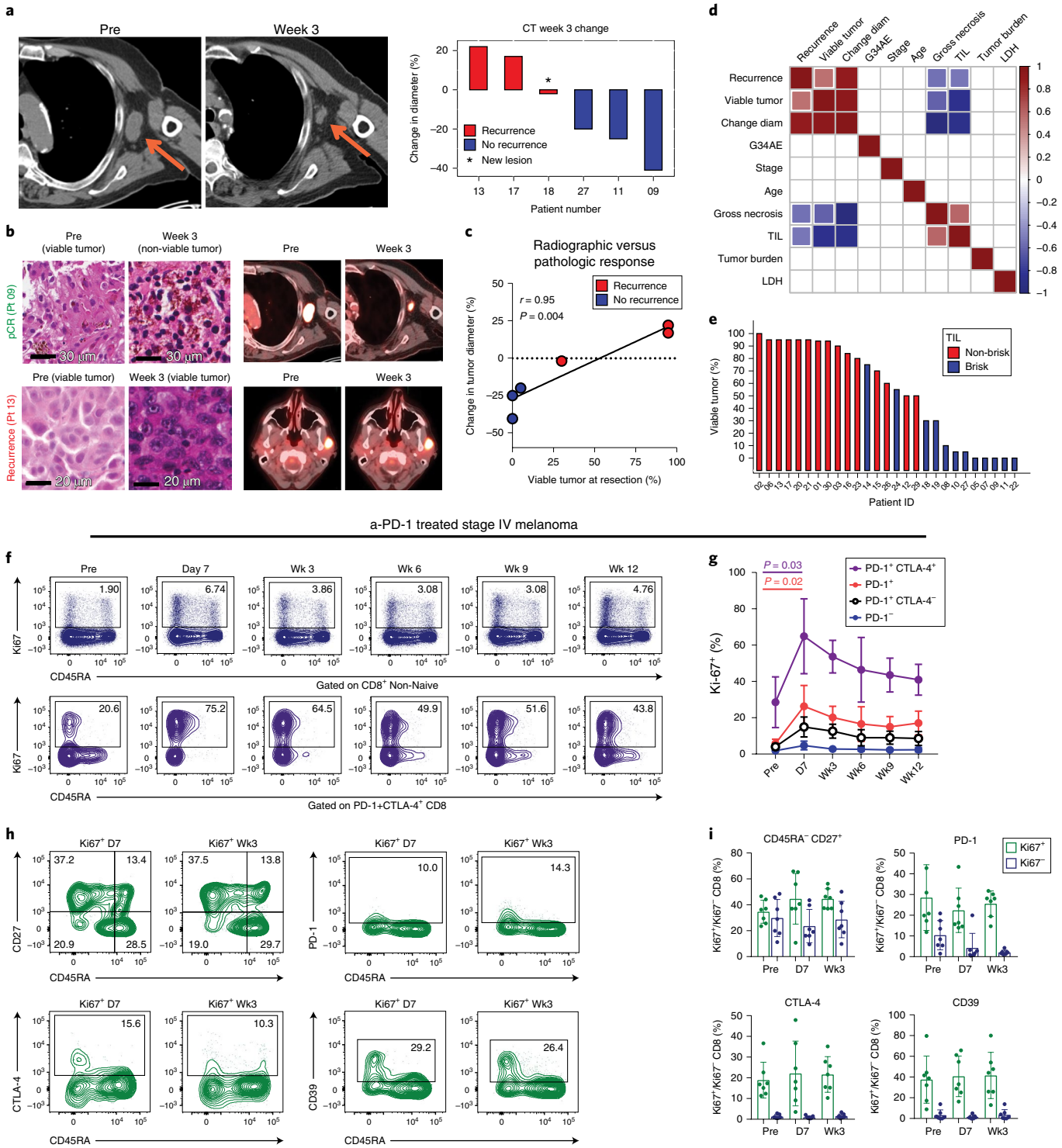

Fig. 2 | Early radiographic, pathologic, and immune response to anti-PD-1. a, Changes in tumor diameter based on the CT portion of FDG PET-CT imaging at 3 weeks compared with pre-treatment colored by recurrence status. **b**, Paired histology and radiographic images from a patient with pCR (top) and a patient with recurrence (bottom). **c**, Correlation of the change in tumor diameter on CT imaging after 1 dose of pembrolizumab versus percentage viable tumor at resection ($n = 6$). *R* score and *P* value generated using Pearson's correlation. **d**, Correlation matrix of selected variables for 27 trial patients with data available at data cut-off. Colored boxes represent Pearson's correlations with a significance of $P < 0.05$. Red to blue represents correlation coefficients ranging from 1 to −1, respectively. **e**, Waterfall plot of percentage of viable tumor colored by TIL infiltration. **f**, Representative flow plots of seven independent patients. **g**, Ki67 expression in CD8 T cell subsets at indicated times ($n = 7$); *P* value calculated using two-sided Wilcoxon matched-pairs test. Error bar denotes mean ± s.d. **h**, Representative flow plots of seven independent patients; gated on Ki67+ CD8. **i**, Percentage expression of markers in Ki67+ (green) or Ki67- (blue) CD8 T cells ($n = 7$ independent patient samples). Error bar denotes mean ± s.d. CT, computed tomography; D, day; ID, identifier; LDH, lactate dehydrogenase; Wk, week.

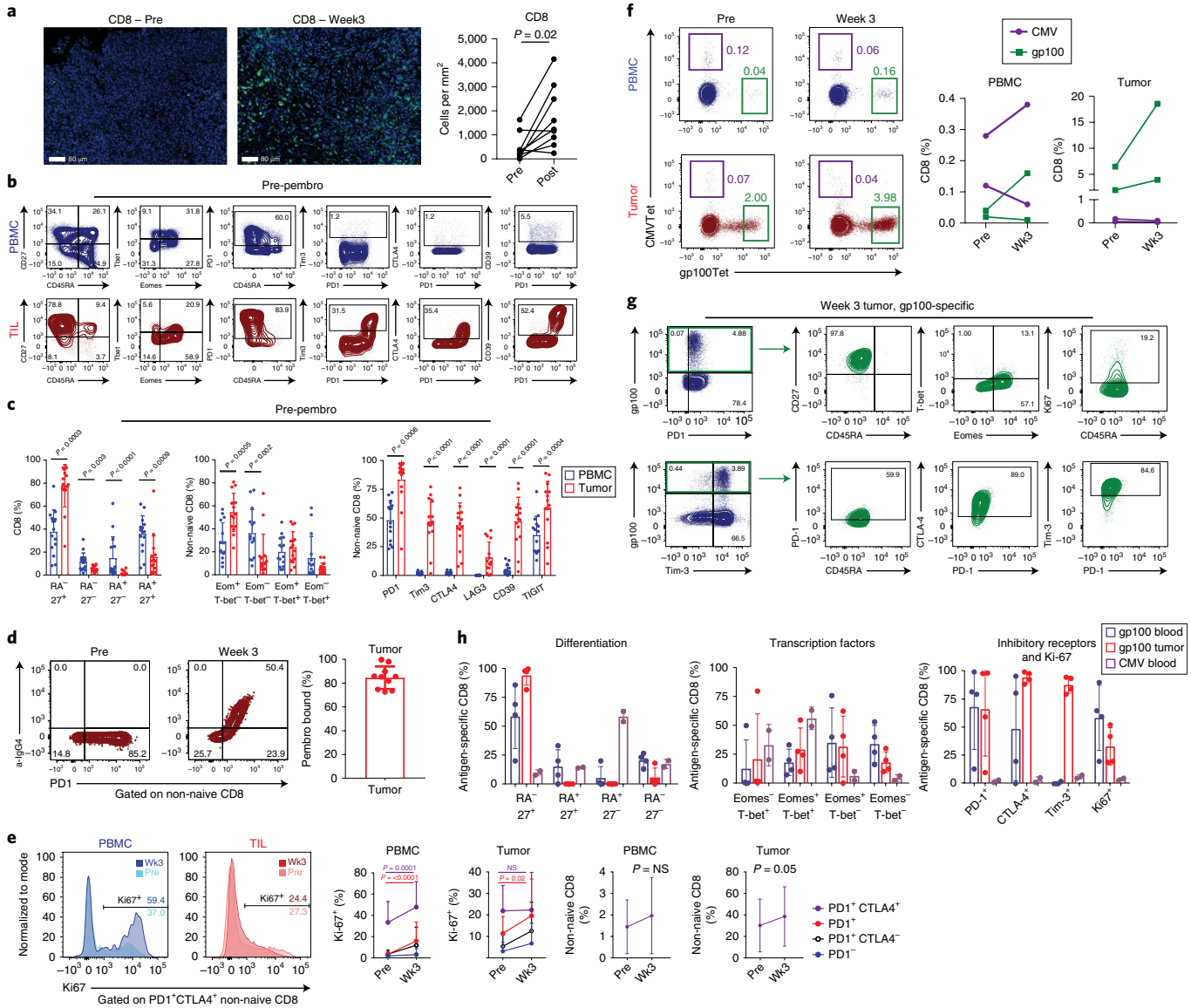

Fig. 3 | Pembrolizumab targets T_{EX} in tumor. a, Changes in tumor CD8 T cells pre- versus post-treatment using immunofluorescence staining ($n=9$ independent paired patient samples; 1 outlier removed due to pretreatment value >2 s.d. above the mean). *P* value calculated using two-sided Wilcoxon matched-pairs test. **b**, Representative flow plots of pretreatment PBMCs and TILs for 15 independent patient samples. Gated on CD8 (CD45RA versus CD27) and non-naïve CD8 (Eomes versus T-bet, CD45RA versus PD-1, PD-1 versus Tim-3, PD-1 versus CTLA-4, PD-1 versus CD39). **c**, Percentages of memory markers, transcription factors, and inhibitory receptors in non-naïve CD8 T cells ($n=15$ independent patient samples). Comparisons for all CD45RA versus CD27 subsets performed using two-sided Wilcoxon matched-pairs test. $Eomes^+T\text{-}bet^-$ comparison performed using two-sided paired *t*-test. $Eomes^-T\text{-}bet^-$ comparison performed using two-sided Wilcoxon matched-pairs test. Comparisons of PD-1 and Lag-3 performed using Wilcoxon matched-pairs test. Comparisons of Tim-3, CTLA-4, CD39, and TIGIT performed using two-sided *t*-test. **d**, Percentage of pembrolizumab bound, calculated by percentage of $IgG4^+$/percentage of PD-1(EH12.1)$^+$ ($n=10$ independent patient samples). Error bar denotes mean ± s.d. **e**, Percentage of Ki67 and frequency of CD8 subsets, pre and at week 3 ($n=28$ independent paired patient samples). *P* values calculated using two-sided Wilcoxon matched-pairs test. Error bars denote mean ± s.d. **f**, Representative flow plots of two paired CMV- and gp100-specific responses pre- and post-treatment, in blood and tumor (left). Frequencies of CMV and gp100 tetramer$^+$ CD8 T cells pre and at week 3 in the blood and tumor (right). **g**, Representative flow plots of memory markers, transcription factors, and IRs for gp100-specific CD8 T cells. **h**, Expression of selected markers in gp100-specific and CMV-specific CD8 T cells at week 3 post-treatment time point ($n=4$ for gp100-specfic responses in blood and tumor; $n=2$ for CMV-specific responses). Error bar denotes mean ± s.d. IR, inhibitory receptor; Pembro, pembrolizumab; RA, CD45RA; 27, CD27.

tumors described in stage IV disease[10,15–17]. Indeed, an 18-gene IFNγ T cell-inflamed signature, GEP18, predictive of clinical response to pembrolizumab in unresectable locally advanced and metastatic cancers[15,18], was also associated with clinical response in our largely stage III setting (Extended Data Fig. 4b). The NRS strongly enriched for the transcriptional signatures[19] from either effector (T_{EFF}) or memory (T_{MEM}) CD8 T cells compared with naïve CD8 T cells (T_{NAIVE}) and also enriched strongly for the signature of T_{EX} from mice[19] (Extended Data Fig. 4c). Moreover, there was a stronger enrichment of the T_{EX} signature when compared directly with T_{EFF} (Fig. 4g), suggesting the importance of pre-existing T_{EX}. In addition, high expression of genes involved in angiogenesis and B cell receptor pathways was associated with clinical benefit (Extended Data Fig. 4d,e), implicating possible

T cell-independent mechanisms of anti-PD-1 response and changes in the tumor microenvironment.

Ten patients have recurred thus far, seven of whom developed distant metastatic disease, two of whom have died (Extended Data Fig. 5a,b). To study mechanisms of resistance, we collected recurrence tumor samples from three patients and compared them with the resection samples (Fig. 4h–k). There was no significant difference in the number of predicted total, or high-quality, neoantigens likely to be recognized by T cell receptors (TCRs) (Extended Data Fig. 5c,d). Patients 01615-06 and 01615-13, however, displayed few CD8 T cells by immunofluorescence, low Ki67, and low percentages of PD-1$^+$or PD-1$^+$CTLA-4$^+$ CD8 T cells in the resection tumor and at progression (Fig. 4i,j). Furthermore, there was a prominent increase in CD163$^+$ myeloid cells with a concomitant decrease in CD3$^+$ cells in both patients (Fig. 4i). Although patient 01615-13 had evidence of T cell activation on progression based on NanoString, there was a concomitant signature of myeloid chemotaxis and activation, including *CD14*, *CCL8*, *CXCL14*, *CLEC5A*, and *CSF1R* (Fig. 4h). Moreover, analysis of whole exome sequencing data revealed a deleterious single-nucleotide variant (SNV) at the *TP53* locus (encoding p53) that was heterozygous at resection (allele frequency of 0.55), but homozygous at recurrence (allele frequency of 0.84; Fig. 4k). P53, a tumor suppressor, may also play a role in immunogenic cell death, CD8 T cell responses, and suppressive myeloid subsets such at MDSCs (myeloid-derived suppresor cells) [20]. Thus, p53 loss may lead to a more aggressive tumor at recurrence and decreased anti-tumor immunity, including increased suppressive myeloid cells. In patient 01615-06, there was little transcriptomic change between resection and recurrence (Fig. 4h); the underlying drivers of progression are unknown. Finally, patient 01615-03 had prominent T cell infiltration post-treatment including many PD-1$^+$CTLA-4$^+$ cells with a high percentage of Ki67$^+$ cells (Fig. 4i,j). This population of cells phenotypically resembled T_{EX} that are associated with positive clinical responses in other settings[3,4,21], suggesting a disconnect between this reinvigorated T_{EX}-like population and the lack of tumor control. Whole exome sequencing, however, revealed loss of heterozygosity in *B2M* on recurrence, with an increase in mutant allele frequency from 0.52 to 0.91 (Fig. 4k), providing a possible explanation for tumor progression despite a vigorous CD8 T cell response to anti-PD-1. Thus, although mechanisms of adaptive resistance have been described that involve mutation, including loss of *B2M*[22–24], suppressive myeloid cells[25], and 'cold tumor' microenvironments[17,26,27], these data highlight the importance of a neoadjuvant approach to potentially identify these mechanisms early on during treatment.

Discussion

Despite the clinical success of checkpoint blockade, we still understand relatively little about the precise mechanism(s) of response or resistance to these treatments. A neoadjuvant approach with anti-PD-1 therapy allowed us to address this question and was feasible and effective in stages IIIB/C and IV melanoma with 63% DFS and 93% overall survival at 2 years. There are several major findings. First, we observed a rapid immune response after PD-1 blockade with T cell reinvigoration peaking 7 days post treatment initiation and complete or major pathologic response in 30% of patients within 3 weeks. Notably, these patients with early complete or major pathological tumor response have 100% DFS at 24 months. In contrast, patients without robust pathological responses at surgery had a poor prognosis with greater than 50% risk of recurrence despite adjuvant therapy. A neoadjuvant approach might allow for early identification of high-risk patients and a change to more effective adjuvant therapy. Second, the data from TILs pre- and post-treatment support a role for CD8 T cells with characteristics of T_{EX}. Finally, these studies provide evidence for mechanisms of response and adaptive resistance including immune failure, immune regulation, and immune escape.

Many patients displayed rapid (3 weeks) complete or nearly complete pathologic responses. These data support the notion that anti-PD-1 revitalizes an already-existing T cell response. In support of this hypothesis are the observations that baseline proliferation of CD8 T cells was associated with clinical benefit and that the immunologic pharmacodynamic response to PD-1 blockade peaked at day 7 after treatment initiation. Although new T cell priming cannot be excluded, this rapidity and robustness favors a model where previously primed CD8 T cells become exhausted and then, on PD-1 blockade, get rapidly reinvigorated. These immune response data are consistent with the rapid anti-tumor responses observed, but also suggest that preventing or avoiding early concomitant immunoregulatory (for example, Treg) and/or later acquired resistance may require combination immunotherapies delivered at times that synergize with this early response to anti-PD-1 therapy.

An obvious question relates to the specificity of the CD8 T cells responding to PD-1 blockade. Previous work has shown that the T_{EX}-phenotype cells in the blood responding to PD-1 blockade were enriched for TCRs also found in TILs[3]. Although it is possible that some of these cells are bystander cells that can be found in blood and tumor, our current studies suggest that CMV-specific CD8 T cells are not likely to respond to anti-PD-1, whereas tumor-specific CD8 T cells targeting gp100 do respond. Moreover, recent work indicates that the PD-1$^+$CD39$^+$ subset of T_{EX} is enriched for tumor-specific T cells compared with the CD39- subset[8] and we find strong enrichment for the CD39$^+$ subset among the cells responding to PD-1 blockade in this cohort. It will be important to extend these types of studies to larger cohorts with detectable shared or neoantigen-specific CD8 T cell populations. However, based on these previous studies, the cells responding to PD-1 blockade in the cohorts analyzed here are likely to be enriched for tumor-specific CD8 T cell populations.

We identified an association between accumulation of T_{EX}-phenotype (Eomes^{hi}T-bet^{lo}) CD8 T cells and clinical benefit. Minimal changes in Ki67 at 3 weeks contrasted with an increased frequency of T_{EX}-like cells in the tumor after anti-PD-1. These

Fig. 4 | Mechanisms of response and resistance to anti-PD-1 therapy. a, Changes in tumor FoxP3$^+$ cells pre- versus post-treatment using immunofluorescence (IF) staining ($n=10$). *P* value calculated using two-sided Wilcoxon matched-pairs test. **b**, Scatter plot of percentage of Ki67$^+$ in non-naïve CD8 versus percentage of Ki67$^+$ in FoxP3$^+$ CD4 (Tregs) at week 3 post-treatment stratified by recurrence status. P13, P06, and P03 represent patients with recurrence tumors, samples analyzed below. Dotted line denotes Treg Ki67$^+$ of 12.4 calculated by CART analysis as the optimal cut point separating recurrence versus no recurrence (left, $n=22$). Kaplan–Maier estimate of DFS stratified according to CART-defined cut-off for Treg Ki67 (right, Ki67 < 12.4, $n=9$; Ki67 ≥ 12.4, $n=13$). *P* value calculated using log-rank test. **c**. Kaplan–Maier estimate of DFS stratified according to CART-defined cut-off for non-naïve CD8 Ki67 at baseline (Ki67 > 5.5, $n=13$; Ki67 ≥ 12.4, $n=8$). *P* value calculated using log-rank test. **d**. Heatmap of 69 differentially expressed genes (NRS) at the pretreatment time point between patients with no recurrence ($n=9$ patients) and recurrence ($n=5$ patients). Differentially expressed genes identified using FDR cut-off of $P=0.05$. **e**, Pathways identified using gene ontology (GO) analysis. **f**, Volcano plot of differentially expressed genes. **g**, GSEA of the NRS; genes that were enriched in T_{EX} versus T_{EFF} cell signatures from Doering et al.[19]. **h**, NanoString gene expression data showing $\log_2$ fold change between progression versus post samples (*x* axis), and expression at progression (*y* axis). **i**, Lymphocyte subsets at post and progression time points by immunohistochemistry (IHC) and IF. **j**, Flow plots of selected markers at post and progression time points for three individual patients. **k**, Integrative Genomics Viewer images corresponding to *B2M* and *TP53* mutations at post and progression time points. Adj, adjusted; CART, classification and regression tree analysis; Eff, effector; Ex, exhausted; FC, fold change; FDR, false discovery rate; N, no; NES, normalized enrichment score; Y, yes.

observations suggest that either reinvigoration in the tumor occurs before week 3, and/or that T_{EX} are reinvigorated peripherally and migrate to the tumor. Indeed, our data demonstrate a peak of T_{EX} reinvigoration in the blood by day 7 and data in mice suggest that immune activity in the tumor occurs early and transiently, whereas a systemic immune response may persist longer[28]. Ki67+ Tregs were also observed in the tumor and correlated with Ki67+ CD8 T cells at week 3. Moreover, proliferation of Tregs was associated with poor DFS. PD-1 blockade may therefore reinvigorate T_{EX} in the tumor but also activate Tregs; the relationship between these changes may be an important feature influencing clinical outcome and an opportunity for Treg-modulating drugs. Analysis of pretreatment tumor also revealed Ki67 expression by non-naïve CD8 T cells as a potential pretreatment biomarker of response. This observation is consistent

with published data in stage IV melanoma where pre-existing CD8 T cells in the tumor are associated with clinical benefit following PD-1 blockade[10]. Our data demonstrate that this pre-existing CD8 T cell immune response is initiated earlier in cancer development (stage III disease). Consistent with this notion, NanoString data demonstrated a distinct inflamed signature before therapy. These observations support the idea that, even in localized disease, the tumor microenvironment is already primed for response or non-response to checkpoint blockade. In patients who recurred, distinct genomic and cellular resistance factors were identified, including *B2M* and *P53* loss of heterozygosity, as well as increased myeloid cell accumulation. Future neoadjuvant studies will allow further study of mechanisms of resistance that may help tailor therapies and/or clinical trials in patients.

Online content

Any methods, additional references, Nature Research reporting summaries, source data, statements of data availability and associated accession codes are available at https://doi.org/10.1038/s41591-019-0357-y.

Received: 9 August 2018; Accepted: 15 January 2019;
Published online: 25 February 2019

References

1. Fridman, W. H., Pages, F., Sautes-Fridman, C. & Galon, J. The immune contexture in human tumours: impact on clinical outcome. *Nat. Rev. Cancer* **12**, 298–306 (2012).
2. Vesely, M. D., Kershaw, M. H., Schreiber, R. D. & Smyth, M. J. Natural innate and adaptive immunity to cancer. *Annu. Rev. Immunol.* **29**, 235–271 (2011).
3. Huang, A. C. et al. T-cell invigoration to tumour burden ratio associated with anti-PD-1 response. *Nature* **545**, 60–65 (2017).
4. Kamphorst, A. O. et al. Proliferation of PD-1^{+} CD8 T cells in peripheral blood after PD-1-targeted therapy in lung cancer patients. *Proc. Natl Acad. Sci. USA* **114**, 4993–4998 (2017).
5. Hellmann, M. D. et al. Pathological response after neoadjuvant chemotherapy in resectable non-small-cell lung cancers: proposal for the use of major pathological response as a surrogate endpoint. *Lancet Oncol.* **15**, e42–e50 (2014).
6. Forde, P. M. et al. Neoadjuvant PD-1 blockade in resectable lung cancer. *N. Engl. J. Med.* **378**, 1976–1986 (2018).
7. Amaria, R. N. et al. Neoadjuvant immune checkpoint blockade in high-risk resectable melanoma. *Nat. Med.* **24**, 1649–1654 (2018).
8. Simoni, Y. et al. Bystander CD8(+) T cells are abundant and phenotypically distinct in human tumour infiltrates. *Nature* **557**, 575–579 (2018).
9. Herbst, R. S. et al. Predictive correlates of response to the anti-PD-L1 antibody MPDL3280A in cancer patients. *Nature* **515**, 563–567 (2014).
10. Tumeh, P. C. et al. PD-1 blockade induces responses by inhibiting adaptive immune resistance. *Nature* **515**, 568–571 (2014).
11. Thommen, D. S. et al. A transcriptionally and functionally distinct PD-1+ CD8+ T cell pool with predictive potential in non-small-cell lung cancer treated with PD-1 blockade. *Nat. Med.* **24**, 994–1004 (2018).
12. Blackburn, S. D. et al. Coregulation of CD8^{+} T cell exhaustion by multiple inhibitory receptors during chronic viral infection. *Nat. Immunol.* **10**, 29–37 (2009).
13. Paley, M. A. et al. Progenitor and terminal subsets of CD8^{+} T cells cooperate to contain chronic viral infection. *Science* **338**, 1220–1225 (2012).
14. Zappasodi, R., Merghoub, T. & Wolchok, J. D. Emerging concepts for immune checkpoint blockade-based combination therapies. *Cancer Cell.* **33**, 581–598 (2018).
15. Ayers, M. et al. IFN-gamma-related mRNA profile predicts clinical response to PD-1 blockade. *J. Clin. Invest.* **127**, 2930–2940 (2017).
16. Harlin, H. et al. Chemokine expression in melanoma metastases associated with CD8^{+} T-cell recruitment. *Cancer Res.* **69**, 3077–3085 (2009).
17. Taube, J. M. et al. Colocalization of inflammatory response with B7-h1 expression in human melanocytic lesions supports an adaptive resistance mechanism of immune escape. *Sci. Transl. Med.* **4**, 127ra137 (2012).
18. Cristescu, R. et al. Pan-tumor genomic biomarkers for PD-1 checkpoint blockade-based immunotherapy. *Science* **362**, eaar3593 (2018).
19. Doering, T. A. et al. Network analysis reveals centrally connected genes and pathways involved in CD8^{+} T cell exhaustion versus memory. *Immunity* **37**, 1130–1144 (2012).
20. Guo, G., Yu, M., Xiao, W., Celis, E. & Cui, Y. Local activation of p53 in the tumor microenvironment overcomes immune suppression and enhances antitumor immunity. *Cancer Res.* **77**, 2292–2305 (2017).
21. Daud, A. I. et al. Tumor immune profiling predicts response to anti-PD-1 therapy in human melanoma. *J. Clin. Invest.* **126**, 3447–3452 (2016).
22. Restifo, N. P. et al. Loss of functional beta 2-microglobulin in metastatic melanomas from five patients receiving immunotherapy. *J. Natl Cancer Inst.* **88**, 100–108 (1996).
23. Sucker, A. et al. Genetic evolution of T-cell resistance in the course of melanoma progression. *Clin. Cancer Res.* **20**, 6593–6604 (2014).
24. Zaretsky, J. M. et al. Mutations associated with acquired resistance to PD-1 blockade in melanoma. *N. Engl. J. Med.* **375**, 819–829 (2016).
25. Engblom, C., Pfirschke, C. & Pittet, M. J. The role of myeloid cells in cancer therapies. *Nat. Rev. Cancer* **16**, 447–462 (2016).
26. Ribas, A. Adaptive immune resistance: how cancer protects from immune attack. *Cancer Discov.* **5**, 915–919 (2015).
27. Teng, M. W., Ngiow, S. F., Ribas, A. & Smyth, M. J. Classifying cancers based on T-cell infiltration and PD-L1. *Cancer Res.* **75**, 2139–2145 (2015).
28. Spitzer, M. H. et al. Systemic immunity is required for effective cancer immunotherapy. *Cell* **168**, 487–502.e15 (2017).

Acknowledgements

Clinical and correlative studies were supported in part by the SPORE in Skin Cancer: P50-CA174523 (X.X., K.L.N., L.M.S., R.K.A., R.M., G.C.K.), P01-CA114046 (X.X.), T32-2T32CA009615 (A.C.H.); the NIH/NCI Cancer Center Support Grant P30-CA016520 (R.K.A., K.L.N., L.M.S., R.M.), and NIH grants AI105343, AI108545, AI117950, AI082630, CA210944 (E.J.W.), and AI114852 (R.S.H.); the Tara Miller Foundation (A.C.H.); the Melanoma Research Alliance (E.J.W.); the David and Hallee Adelman Immunotherapy Research Fund (E.J.W.); the Heisenberg program BE5496/2-1 of the DFG (B.B.); and the Parker Institute for Cancer Immunotherapy Bridge Scholar Award (A.C.H.). Merck, Inc. supplied drugs and supported clinical and translational aspects of this study. The Human Immunology Core and the Tumor Tissue and Biospecimen Bank of the University of Pennsylvania (supported by P30-CA016520) assisted in tissue collection, processing, and storage.

Author contributions

A.C.H., T.C.M., and E.J.W. conceived and designed the overall studies. A.C.H. and T.C.M. designed the clinical trial at Penn. A.C.H., T.C.M., R.J.O., X.X., M.D.F., and G.C.K. implemented the clinical trial at Penn, and T.C.M. was principal investigator of this clinical trial. X.X. and S.L. performed pathologic response and TIL assessments. A.C.H., R.J.O., P.K.Y., S.M.G., B.B., and R.S.H. performed immune assessment assays. A.C.H., R.J.O., P.K.Y., S.M.G., and M.W.K. analyzed immune assessment data. R.Mick performed biostatistical analyses. S.Manne, Q.Z., W.M.B., R.Mogg, and J.H.Y. performed NanoString assay and/or computational analysis of NanoString data. A.A.K., L.D., B.M.W., B.W., K.D'A., and K.L.N. performed mutational analysis and neoepitope prediction. W.X., L.G., M.C., S.McGettigan, and K.K. assisted in the Penn clinical trial. A.K. and M.D.F. performed radiographic assessments. L.A. and J.H.Y. performed and/or analyzed immunohistochemistry and immunofluorescent assays. G.P.L., R.K.A., G.C.K., M.D.F., and L.M.S. were investigators on the trial. A.C.H., T.C.M., and E.J.W. interpreted the data. A.C.H., T.C.M., and E.J.W. wrote the manuscript. E.J.W. and T.C.M. designed, interpreted, and oversaw the study.

Competing interests

Merck provided funding and drugs for the clinical trial. Merck performed immunohistochemistry, immunofluorescence, and NanoString assays, and played a role in the analysis of these data. Merck played no role in the design, data collection, decision to publish, or preparation of the manuscript. R.J.O. was at Penn while engaged in this project, but is now currently employed at Merck. L.A., Q.Z., R.M., W.M.B., and J.H.Y. are currently or were employed at Merck when engaged in this project. E.J.W. is a member of the Parker Institute for Cancer Immunotherapy which supported the UPenn cancer immunotherapy program. E.J.W. has consulting agreements with and/or is on the scientific advisory board for Merck, Roche, Pieris, Elstar, and Surface Oncology. E.J.W. has a patent licensing agreement on the PD-1 pathway with Roche/Genentech. E.J.W. is a founder of Arsenal Biosciences. T.C.M. has had advisory roles with Bristol-Myers Squibb, Merck, Incyte, Aduro Biotech, and Regeneron.

Additional information

Extended data is available for this paper at https://doi.org/10.1038/s41591-019-0357-y.

Supplementary information is available for this paper at https://doi.org/10.1038/s41591-019-0357-y.

Reprints and permissions information is available at www.nature.com/reprints.

Correspondence and requests for materials should be addressed to A.C.H., E.J.W. or T.C.M.

Publisher's note: Springer Nature remains neutral with regard to jurisdictional claims in published maps and institutional affiliations.

Methods

Study design and patient population. This phase 1b clinical trial (NCT02434354) was a single institution investigator-initiated study sponsored by the University of Pennsylvania. The protocol and its amendments were approved by the Institutional Review Board at the University of Pennsylvania, and all patients provided written informed consent. Patients were eligible for enrollment if they were 18 years of age or older, had an Eastern Cooperative Group performance status of 0 or 1, had adequate organ function according to protocol criteria, and had measurable resectable clinical stage III or resectable stage IV melanoma. Patients had to have an adequate tumor size, in the opinion of the surgical oncologist and study team, to allow for collection of biopsy tissue equivalent to at least two to four core biopsies for the pretreatment biopsy, with an expectation that an equal or greater amount of tissue would remain after biopsy. Patients could not have received previous ipilimumab or other immune therapies. Previous BRAF-directed therapies were permitted. Patients with uveal or mucosal melanoma were not eligible, nor were patients on systemic steroids or immunosuppression, patients who had received radiation to the resectable tumor, or patients with active brain metastasis.

Treatment and assessment. After obtaining informed consent, all patients underwent a baseline pretreatment biopsy, which consisted of the equivalent amount of tissue of at least two to four core biopsies. Patients then received a single flat dose of pembrolizumab 200 mg intravenously, followed by complete resection 3 weeks later. Patients also provided paired blood samples at the pretreatment and post-treatment time points. After resection and on surgical recovery, patients continued to receive adjuvant pembrolizumab every 3 weeks for up to 1 yr, or until the time of recurrence or any unacceptable treatment-related toxicity (Fig. 1a). Both the biopsies and the resection specimens were processed in the Department of Pathology and Laboratory Medicine, Hospital of the University of Pennsylvania, and immediately snap or formalin fixed and paraffin embedded, with a portion of unfixed tissue allocated for extraction of TILs for translational studies. Gross photos were taken of resection specimens. Patients were assessed for pathologic response at the 3-week resection time point, with the resection tumor assessed for percentage of viable tumor by a melanoma pathologist. Complete pathologic response was defined as the absence of viable tumor based on hematoxylin and eosin (H&E) staining. A major pathologic response was defined as less than 10% of viable tumor. Pre- and post-treatment tumors were also assessed for TIL infiltration and scored as either brisk (diffuse lymphocytes throughout the tumor), non-brisk (only foci of lymphocytes), or absent[29]. Imaging (PET-CT or computed tomography of the chest, abdomen, and pelvis) was performed at baseline and on study. Patients were assessed for recurrence and followed for DFS and overall survival. Grading of adverse events was performed using the Common Terminology Criteria of Adverse Events version 4. The objective of this report is to examine the pCR rate at the time of resection after one dose of pembrolizumab, and to evaluate pathologic response as a predictor of DFS. To date, 29 patients have received treatment on the trial and are included in this analysis.

Statistical analysis. The primary objectives of the clinical trial are to establish safety and obtain paired tissue samples for analysis of immunologic effects. The target sample size was 30 patients. If 5 or fewer of 30 patients experienced a severe (grade 3 or higher) adverse event that was not attributable to pembrolizumab or to surgery alone, then safety was established since the true toxicity rate is probably no higher than 30% based on the upper bound of the 2-sided 95% confidence interval.

A secondary objective of the trial was to study the biological changes in paired tumor tissue specimens before and in the presence of anti-PD-1. For this report, the primary end point was DFS from the date of definitive surgery to first documented disease recurrence, death due to any cause, or last patient contact documenting disease-free status. The rate of pathologic response (defined as complete or major pathologic response[5,6]) and exact 95% confidence interval were estimated for 29 patients who have enrolled and undergone surgery on the trial. Median potential follow-up was estimated by the reverse Kaplan–Meier method. DFS from landmark date of definitive surgery to first documented disease recurrence, death due to any cause, or last patient contact documenting disease-free status was estimated by the Kaplan–Meier method. Cox proportional hazards regression modeling was employed to estimate the magnitude of effect of pathologic response on DFS. Multivariable models were employed to adjust for established prognostic factors. Unadjusted and adjusted hazard ratios and their 95% confidence intervals were estimated. To address the low event rate in the group with pCR and the group with brisk TILs post-treatment, we applied Firth's penalized regression method for the Cox proportional hazard model, with the penalized likelihood ratio test[30]. For normal data, parametric Student's *t*-test and paired *t*-test were used for unpaired and paired analyses, respectively. For non-normal data, non-parametric Mann–Whitney or Wilcoxon matched-pairs signed rank tests were used for unpaired and paired analyses, respectively. Correlations between continuous variables were determined by Pearson's *r* coefficient. Fisher's exact test was employed to test for association between two categorical variables. McNemar's test was used to test concordance between paired categorical variables to determine treatment effect (that is, pretreatment and post-treatment TIL score). Statistical analyses were performed using either IBM SPSS v23, R, or Graphpad Prism.

Sample processing: PBMCs and tumor. Patient blood was drawn in sodium heparin tubes, kept at room temperature, and processed within 8 h of blood draw. Whole blood was centrifuged and plasma samples were collected, aliquoted in the volume of 1 ml per cryotube, and stored at -80 °C. Blood samples were reconstituted by adding an equal volume of Hank's balanced salt solution (HBSS, Corning MT21021CM) to the volume of collected plasma. Reconstituted blood samples were diluted two-fold in HBSS and Ficoll (Ficoll-Paque PLUS density gradient medium, GE Healthcare Life Sciences, 17-1440-03) was layered underneath. The volume of Ficoll-Paque PLUS used was equal to that of the undiluted blood sample. The buffy coat was collected and washed twice with HBSS. Ammonium-chloride-potassium lysis buffer (Lonza 10-548E) was used to lyse the red blood cells, if necessary. Melanoma tumor samples were processed within 4 h after excision from the patient. Samples were cut into 2–3-mm pieces with a scalpel in an RPMI 1640 (Corning 10-040-CM)-containing petri dish. A 70-µm cell strainer (Falcon 352350) was placed on top of a 50-ml conical tube and the tissue fragments were transferred to the cell strainer with a pipette. The cells were released by gently grinding the tissue fragments using the thumb depressor of a sterile syringe plunger placed against the cell strainer. Cells were washed twice and counted in a hemocytometer. The numbers of lymphocytes and melanoma cells were distinguished by their morphology and recorded separately.

Flow cytometry. Fresh trial PBMCs and tumor suspension were stained with a master mix of antibodies for surface stains including CD4 (Biolegend, OKT4), CD8 (BD, RPA-T8), CD45RA (Biolegend, HI100), Tim-3 (Biolegend, F38-2E2), Lag3 (3DS223H, eBioscience), CD39 (Biolegend, A1), CD27 (BD, L128), and PD-1 (BD, EH12.1) and intracellular stains for FoxP3 (BD, 259D/C7), CTLA-4 (BD, BNI3), Eomes (eBioscience, WD1928), T-bet (Biolegend, 4B10), and Ki67 (BD, B56). HLA-A2 tetramers were generated at the National Institutes of Health tetramer facility for the melanoma gp100 peptide G280 (YLEPGPVTV) and CMV peptide pp65 (NLVPMVATV). Permeabilization was performed using the Foxp3 Fixation/Permeabilization Concentrate and Diluent kit (eBioscience). PD-1 on post-pembrolizumab specimens was detected using anti-human IgG4 phycoerythrin (Southern Biotec) as previously described[3,31]. Cells were resuspended in 1% para-formaldehyde until acquisition on a BD Biosciences LSR II cytometer and analyzed using FlowJo (Tree Star).

Immunohistochemical staining and scoring of PD-L1 (single chromogenic). Whole tissue sections cut from formalin-fixed paraffin-embedded (FFPE) tissue blocks were deparaffinized and rehydrated with serial passage through changes of xylene and graded ethanols. All slides were subjected to heat-induced epitope retrieval in Envision FLEX Target Retrieval Solution, High pH (Dako). Endogenous peroxidase in tissues was blocked by incubation of slides in 3% hydrogen peroxide solution before incubation with primary antibody (anti-PD-L1, clone 22C3, Merck Research Laboratories, or anti-PD-1 clone NAT105, Cell Marque) for 60 min. Antigen-antibody binding was visualized via application of the FLEX+ polymer system (Dako) via application of mouse Envision system, and application of 3, 3' diaminobenzidine chromogen (Dako). Stained slides were counterstained with hematoxylin and cover slipped for review. Scoring of PD-L1 was conducted by a pathologist blinded to patient characteristics and clinical outcomes[32]. A semiquantitative 0–5 scoring system was applied: negative, 0; rare, 1—individuated positive cells or only very small focus within or directly adjacent to tumor tissue; low, 2—infrequent small clusters of positive cells within or directly adjacent to tumor tissue; moderate, 3—single large cluster, multiple smaller clusters, or moderately dense diffuse infiltration, within or directly adjacent to tumor tissue; high, 4—single very large dense cluster, multiple large clusters, or dense diffuse infiltration; very high, 5—coalescing clusters, dense infiltration throughout the tumor tissue.

Immunofluorescent staining and image acquisition. Multiplexed immunofluorescent staining was performed on a Dako autostainer (Agilent). The FFPE sections were rehydrated in a series of graded alcohols to distilled water. Antigen retrieval was performed in Target Retrieval Solution (TRS) citrate buffer (pH 6.0) using a pressure cooker. The slides were blocked in 1% casein blocking buffer for 30 min, followed by incubation with primary antibody for 1 h. Slides were incubated with polymer horseradish peroxidase-secondary antibody for 30 min followed by application of fluorophore-4 tyramide signal amplification dye (Opal 7 color kit, PerkinElmer). After detection of first primary antibody, the slides were stripped of any primary and secondary antibodies by treating the slides in AR6 (Perkin Elmer) antibody-stripping buffer in a microwave oven. Sequentially, the slides were stained with second or third primary antibody and the process was repeated. Nuclear staining was carried out with DAPI followed by cover slipping. CD8xFoxP3xCD163 triplex staining was accomplished with PerkinElmer Opal kit (PerkinElmer). CD8, FoxP3, and CD163, labeled with Opal fluorophores 690, 570, and 520, respectively, were sequentially applied to the tissue sections. CD8xCD3 duplex immunofluorescent staining was accomplished with Thermo Fisher Scientific Tyramide Signal Amplification kit (Thermo Scientific). The sequence for antibody staining is CD8 and CD3, labeled with Alexa fluorophores 488 and 568, respectively. Epifluorescence multispectral whole slide images of all sections were acquired through the Vectra 3.0 Automated Quantitative Pathology Imaging

System (PerkinElmer) at ×10 and ×20 magnifications. Quantitative image analyses were carried out on ×10 images using Halo Highplex FL module (Indica Labs).

Preparation of FFPE RNA isolation and gene expression analysis using the NanoString nCounter system. RNA was isolated from slides of FFPE tissue for analysis on the NanoString nCounter gene expression platform (NanoString Technologies). Before RNA isolation, tissue sections were deparaffinized in xylene for 3×5 min, then sequentially rehydrated in 100% ethanol for 2×2 min, 95% ethanol for 2 min, and 70% ethanol for 2 min, and then immersed in distilled H_2O until ready to be processed. Tissue was lysed on the slide by adding 10–50 µl PKD buffer (Qiagen catalog no. 73504). Tissue was then scraped from the slide and transferred to a 1.5-ml Eppendorf tube. Proteinase K (Roche catalog no. 03115836001) was added at no more than 10% final volume and the RNA lysate was incubated for 15 min at 55 °C and then 15 min at 80 °C. RNA was isolated using the Qiagen RNeasy FFPE kit per manufacturer protocol (Qiagen). Sample concentration was measured on the NanoDrop Spectrophotometer (Thermo Fisher) per manufacturer protocol. The resulting total RNA was stored at −80 °C until gene expression profiling was performed using the NanoString nCounter system. Per sample, 50 ng total RNA isolated from FFPE tissue was mixed with a 3′ biotinylated capture probe and a 5′ reporter probe tagged with a fluorescent barcode, from a custom-designed gene expression code set. Probes and lysate were hybridized overnight at 65 °C for 12–16 h. Hybridized samples were then run on the NanoString preparation station using their high-sensitivity protocol per manufacturer instructions (NanoString Technologies). The samples were scanned at maximum scan resolution capabilities using the nCounter Digital Analyzer (NanoString Technologies). All sample and data normalization occurred within the nCounter digital analyzer software, nSolver. Specifically, the raw code count data were normalized using a positive control normalization factor based on the spiked-in positive control raw counts and also a content normalization factor derived from the raw counts of a set of relevant housekeeping genes. Transcripts with counts less than or equal to the highest embedded negative controls (background noise) in that sample are first set to its background. The gene count for each gene is then subtracted from this background so that each sample has the same footing where zero numbers represent undetectable noise.

NanoString gene expression analysis. R package limma_3.34.9 was used to do pair wise comparisons of the normalized NanoString gene expression data. R package pheatmap_1.0.10 was used for creating heatmaps to display NanoString gene expression data. Metascape.org was used to enrich genes for gene ontology biological processes. Gene set enrichment analysis (GSEA)[33,34] used to check for enrichment of gene signatures from microarray data in the NanoString data. The 18-gene T cell-inflamed gene expression profile (GEP) was developed as described by Ayers et al. and comprises genes related to antigen presentation, chemokine expression, cytolytic activity, and adaptive immune resistance[15]. These genes are as follows: *CCL5*, *CD27*, *CD274 (PD-L1)*, *CD276 (B7-H3)*, *CD8A*, *CMKLR1*, *CXCL9*, *CXCR6*, *HLA-DQA1*, *HLA-DRB1*, *HLA-E*, *IDO1*, *LAG3*, *NKG7*, *PDCD1LG2 (PDL2)*, *PSMB10*, *STAT1*, *TIGIT*. The GEP score was computed by taking a weighted sum of the housekeeping normalized values of the 18 genes on the GEP18 signature.

DNA isolation and exome sequencing. Whole exome sequencing was performed on FFPE tumor tissue with matched germline DNA. Manual macrodissection was performed on FFPE slides, if necessary, using a scalpel and an H&E-stained slide as a guide. Tissue deparaffinization and DNA extraction were performed using standard methods. DNA was quantified using Qubit dsDNA BR Assay (Invitrogen) and sheared to an average of 250 base pairs (bp) with the Covaris LE220 ultrasonicator (Covaris). For genomic library preparation, paired-end libraries were prepared using the NEBNext Ultra Kit (New England Biolabs) and DNA library quality and fragment size were measured with an Agilent 2100 Bioanalyzer. Exome sequences were enriched from the genomic libraries according to the manufacturer protocol with the SureSelectXT2 Human All Exon V6+COSMIC (Agilent). Samples were pooled and sequenced on the Illumina HiSeq 4000 with 150-bp paired-end reads with an average target depth of 87×.

Bioinformatic analysis of whole exome sequencing data. Fastq data for tumor and matched normal DNA were aligned to the Genome Reference Consortium Human Build 37 using the Burrows–Wheeler aligner[35]. Resultant bam files were further processed following Genome Analysis Toolkit Best Practices[36,37]. Somatic SNVs and indels were detected using Mutect2 (MuTect2 is a somatic SNP and indel caller that combines the DREAM challenge-winning somatic genotyping engine of the original MuTect[38] with the assembly-based machinery of HaplotypeCaller) included as part of Genome Analysis Toolkit v4.0.7.0. Lower confidence variants, determined from cross-sample contamination estimates and sequence context-dependent artifacts, were filtered out from the somatic VCF files. Copy number alterations and regions displaying allele-specific loss of heterozygosity were determined using Sequenza[39]. Unique somatic SNVs and indel mutations in post-therapy versus progression samples were determined by pair wise overlap analysis implemented in data.table in R. Further, allele frequencies for mutations common to both post-therapy and progression samples were investigated for changes in zygosity.

Neoantigen analysis. VCF files containing somatic non-synonymous SNVs and indels passing two-stage filtering from Mutect2 were annotated for wild-type peptide sequence using the Wildtype plugin from ensembl-Variant Effect Predictor (v.92.0). Further, the downstream effects of frameshift variants on the protein sequence were determined using the Downstream plugin from ensembl-Variant Effect Predictor. Prediction of HLA-binding neoantigens ranging from 9 to 11 amino acids in length was accomplished using NetMHCcons[40] implemented within pVacSeq[41]. Neoantigens were subsequently filtered by the predicted binding dissociation constant ($k_D \leq 500$ nM) and by agretopicity, requiring that mutant peptides have greater binding affinities than their corresponding wild-type sequences. All 9-mers were then analyzed for their likelihood of TCR recognition using a thermodynamic neoantigen fitness model, as previously described[42]. Neoantigen loads for all 9–11-mers filtered by dissociation constant and agretopicity described above as well as neoantigens likely to be recognized by TCRs were plotted using the ggplot2 package within R (v.3.5.0). Further, loss of TCR-recognized neoantigens from post-therapy to progression was determined by pair wise overlap analysis implemented in the data.table package in R.

Reporting Summary. Further information on research design is available in the Nature Research Reporting Summary linked to this article.

Code availability

Custom code used to analyze tumor whole exome sequencing data is available at https://zenodo.org/badge/latestdoi/162582612

Data availability

NanoString data that support the findings have been deposited in the NCBI Gene Expression Omnibus and are accessible through GEO Series accession number GSE123728. DNA whole exome sequencing data have been deposited in SRA and are accessible under SRA accession number PRJNA510621. All other relevant data are available from the corresponding author upon reasonable request.

References

29. Mihm, M. C. Jr., Clemente, C. G. & Cascinelli, N. Tumor infiltrating lymphocytes in lymph node melanoma metastases: a histopathologic prognostic indicator and an expression of local immune response. *Lab. Invest.* **74**, 43–47 (1996).
30. Heinze, G. & Schemper, M. A solution to the problem of monotone likelihood in Cox regression. *Biometrics* **57**, 114–119 (2001).
31. Brahmer, J. R. et al. Phase I study of single-agent anti-programmed death-1 (MDX-1106) in refractory solid tumors: safety, clinical activity, pharmacodynamics, and immunologic correlates. *J. Clin. Oncol.* **28**, 3167–3175 (2010).
32. Chen, M. et al. Development and validation of a novel clinical fluorescence in situ hybridization assay to detect JAK2 and PD-L1 amplification: a fluorescence in situ hybridization assay for JAK2 and PD-L1 amplification. *Mod. Pathol.* **30**, 1516–1526 (2017).
33. Subramanian, A. et al. Gene set enrichment analysis: A knowledge-based approach for interpreting genome-wide expression profiles. *Proc. Natl. Acad. Sci. USA* **102**, 15545–15550 (2005).
34. Mootha, V. K. et al. PGC-1alpha-responsive genes involved in oxidative phosphorylation are coordinately downregulated in human diabetes. *Nat. Genet.* **34**, 267–273 (2003).
35. Li H. Aligning sequence reads, clone sequences and assembly contigs with BWA-MEM. Preprint at arXiv:1303.3997v2 [q-bio.GN] (2013), https://arxiv.org/abs/1303.3997.
36. DePristo, M. et al. A framework for variation discovery and genotyping using next-generation DNA sequencing data. *Nat. Genet.* **43**, 491–498 (2011).
37. Van der Auwera, G. A. et al. From fastq data to high-confidence variant calls: the genome analysis toolkit best practices pipeline. *Curr. Protoc. Bioinformatics* **43**, 11.10.1–11.10.33 (2013).
38. Cibulskis, K. et al. Sensitive detection of somatic point mutations in impure and heterogeneous cancer samples. *Nat. Biotechnol.* **31**, 213–219 (2013).
39. Favero, F. et al. Sequenza: allele-specific copy number and mutation profiles from tumor sequencing data. *Ann. Oncol.* **26**, 64–70 (2015).
40. Karosiene, E., Lundegaard, C., Lund, O. & Nielsen, M. NetMHCcons: a consensus method for the major histocompatibility complex class I predictions. *Immunogenetics* **64**, 177–186 (2012).
41. Hundal, J. et al. pVAC-Seq: a genome-guided in silico approach to identifying tumor neoantigens. *Genome Med.* **8**, 11 (2016).
42. Luksza, M. et al. A neoantigen fitness model predicts tumour response to checkpoint blockade immunotherapy. *Nature* **551**, 517–520 (2017).

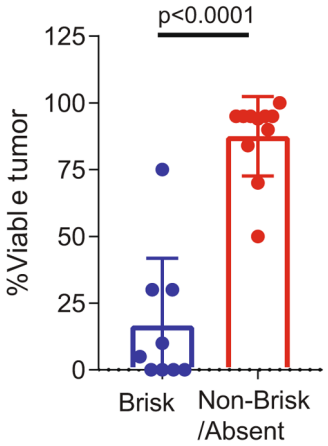

Extended Data Fig. 1 | TIL score associated with pathologic response. Percentage viable tumor between brisk ($n=9$) versus non-brisk/absent tumors ($n=11$). *P* value calculated using two-sided Mann–Whitney test.

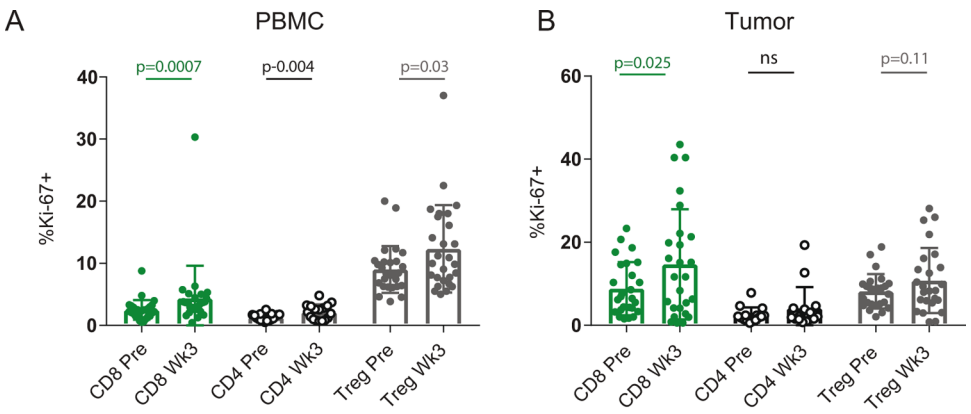

Extended Data Fig. 2 | Immune response to anti-PD-1 for T cell subsets in blood and tumor. a, Percentage Ki67 expression in CD8, conventional CD4, and Treg (FoxP3$^+$ CD4) T cells pre and post in blood ($n=28$ independent paired patient samples for CD8 comparisons, $n=17$ independent paired patient samples for CD4 comparisons, and $n=27$ independent patient samples for Treg comparisons). Two-sided Wilcoxon matched-pairs test was performed for CD8 and Treg comparisons. Two-sided *t*-test was performed for CD4 comparison. **b**, Percentage Ki67 expression in CD8, conventional CD4, and Treg (FoxP3$^+$ CD4) T cells pre and post in tumor ($n=26$ independent paired patient samples for CD8 comparisons, $n=15$ independent paired patient samples for CD4 comparisons, and $n=25$ independent paired patient samples for Treg comparisons). Two-sided Wilcoxon matched-pairs test was performed for CD4 and Treg comparisons. Two-sided *t*-test was performed for CD8 comparison.

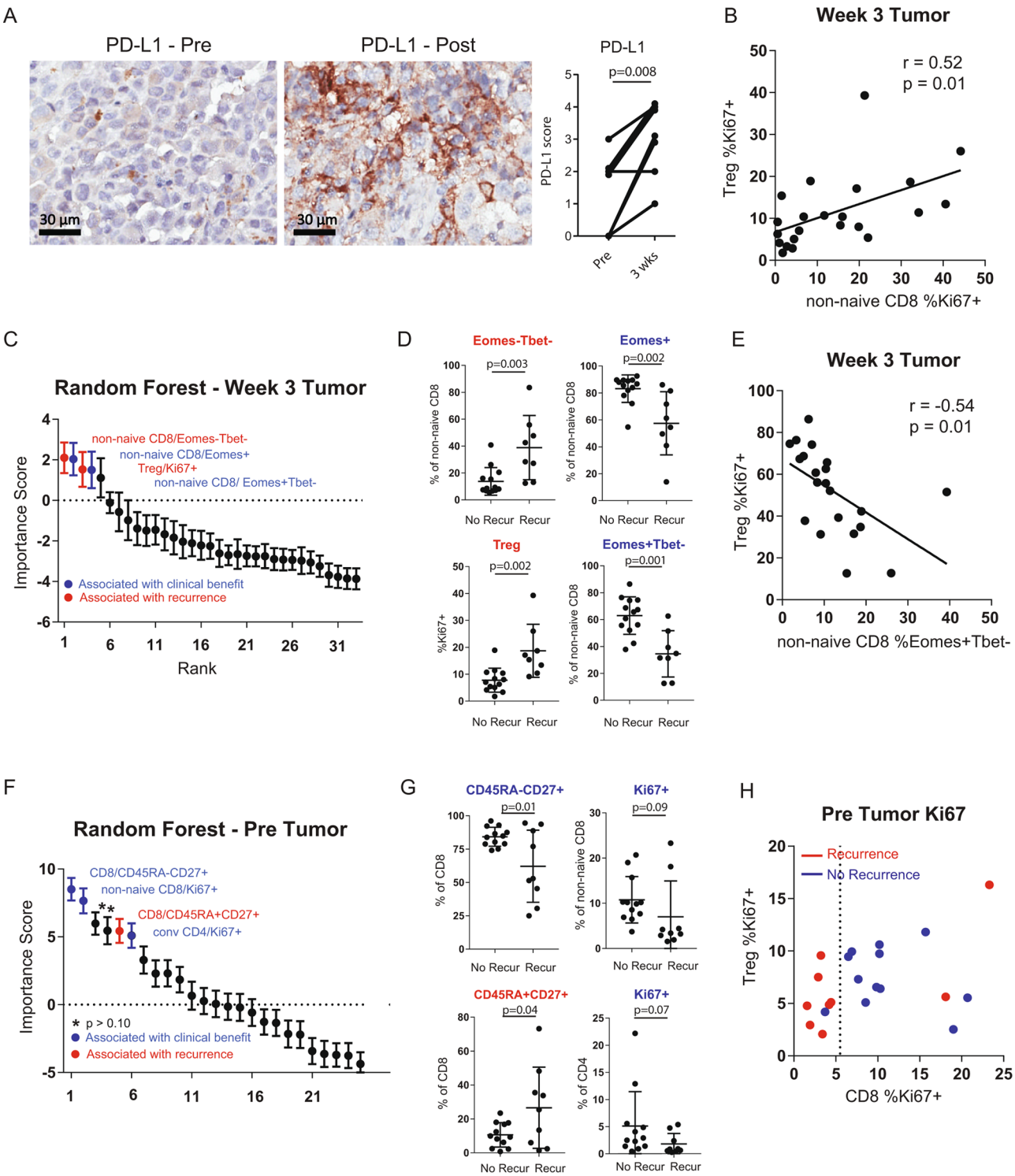

Extended Data Fig. 3 | See figure caption on next page.

Extended Data Fig. 3 | Cellular determinants of response and resistance to anti-PD-1. a, Changes in tumor PD-L1 pre- versus post-treatment using immunohistochemistry staining ($n = 9$ independent paired patient samples). $^{**}P < 0.01$ using two-sided Wilcoxon matched-pairs test. **b**, Correlation of percentage of $Ki67^+$ in non-naïve CD8 T cells versus percentage of $Ki67^+$ in Tregs ($FoxP3^+CD4$) ($n = 21$ independent patient samples); *R* score and *P* value generated using Pearson's correlation. **c**, Thirty-three post-treatment immune parameters classified by recurrence using random forest analysis and ranked by importance score ($n = 21$ independent patient samples). Error bar denotes mean ± s.d. for 1,000 random forest iterations. **d**, Percentage expression of selected markers in tumor between patients with recurrence (9 independent patient samples) and no recurrence (12 independent patient samples). *P* value calculated using two-sided Mann–Whitney test. **e**, Correlation of percentage of $Ki67^+$ in Tregs ($FoxP3^+$ CD4) versus percentage of $Eomes^+$ $T\text{-}bet^-$ in non-naïve CD8 ($n = 21$ independent patient samples); *R* score and *P* value generated using Pearson's correlation. **f**, Twenty-five pretreatment immune parameters classified by recurrence using random forest analysis and ranked by importance score ($n = 21$ independent patient samples). Error bar denotes mean ± s.d. for 1,000 random forest iterations. **g**, Percentage expression of selected markers in tumor between patients with recurrence (9 independent patient samples) and no recurrence (12 independent patient samples). Two-sided *t*-test was used for $CD45RA^-CD27^+$ and $CD45RA^+CD27^+$ comparisons. Two-sided Mann–Whitney test was used for CD8 $Ki67^+$ and CD4 $Ki67^+$ comparisons. Error bar denotes mean ± s.d. **h**, Scatter plot of percentage of $Ki67^+$ in non-naïve CD8 versus percentage of $Ki67^+$in $FoxP3^+$ CD4 (Tregs) at pretreatment stratified by recurrence status. Dotted line denotes non-naïve CD8 $Ki67^+$ of 5.5 calculated by CART analysis as the optimal cut point separating recurrence versus no recurrence ($n = 21$ independent patient samples).

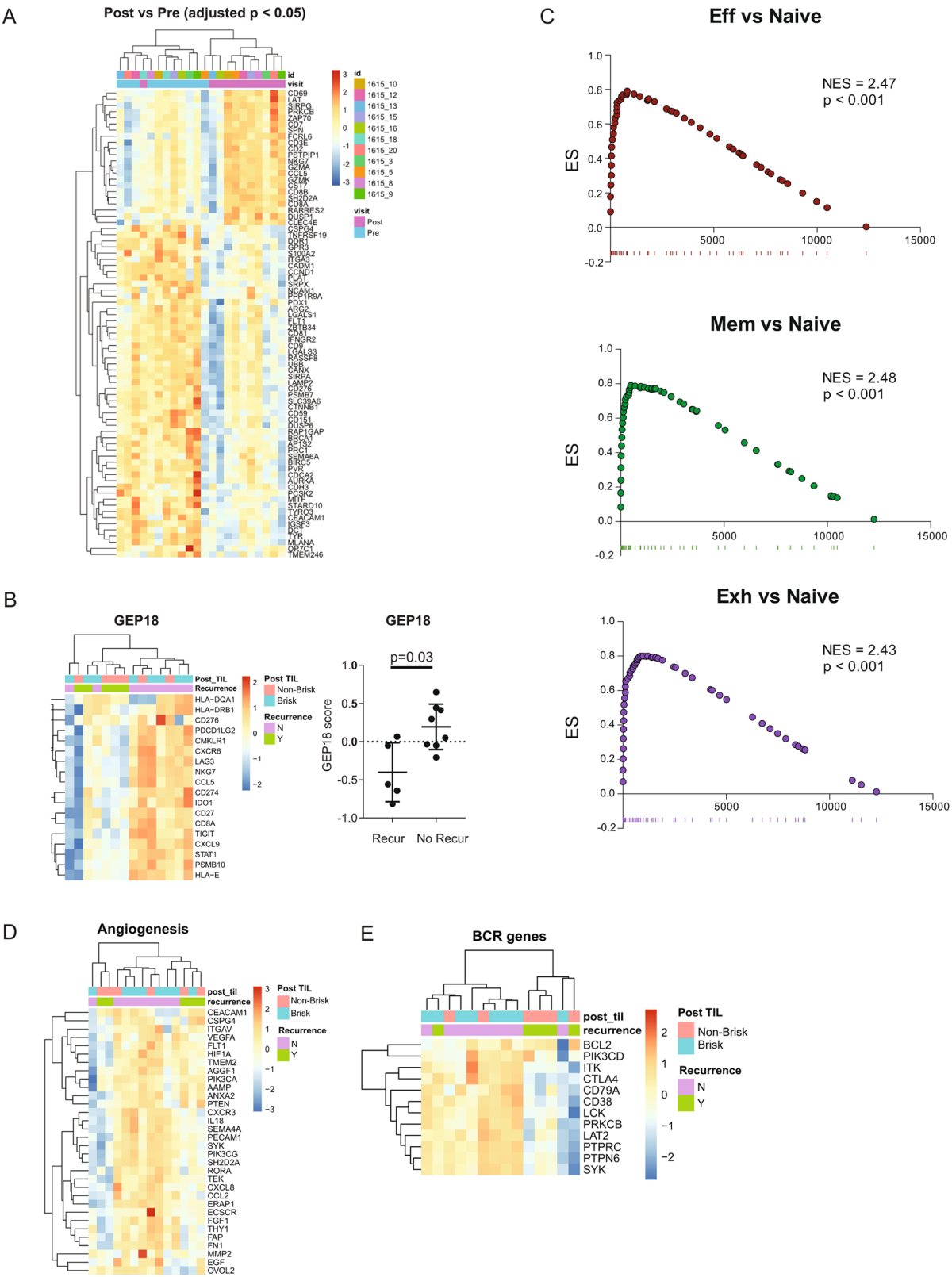

Extended Data Fig. 4 | Immune signatures associated with clinical response. a, Heatmap of differentially expressed genes between pretreatment and post-treatment tumor ($n = 11$ independent paired patient samples). Differentially expressed genes identified using an FDR cut-off of $P = 0.05$ after adjusting for multiple comparisons. **b**, Heatmap and GEP score between patients with recurrence ($n = 5$ independent patient samples) and no recurrence ($n = 8$ independent patient samples). *P* value calculated using two-sided Mann–Whitney test. Error bar denotes mean ± s.d. **c**, GSEA of NRS genes that were enriched in T_{EFF}, T_{MEM}, and T_{EX} versus T_{NAIVE} cell signatures from ref. [19]. **d**, Heatmap of angiogenesis-associated genes from gene ontology. **e**, Heatmap of B cell receptor-associated genes from gene ontology.

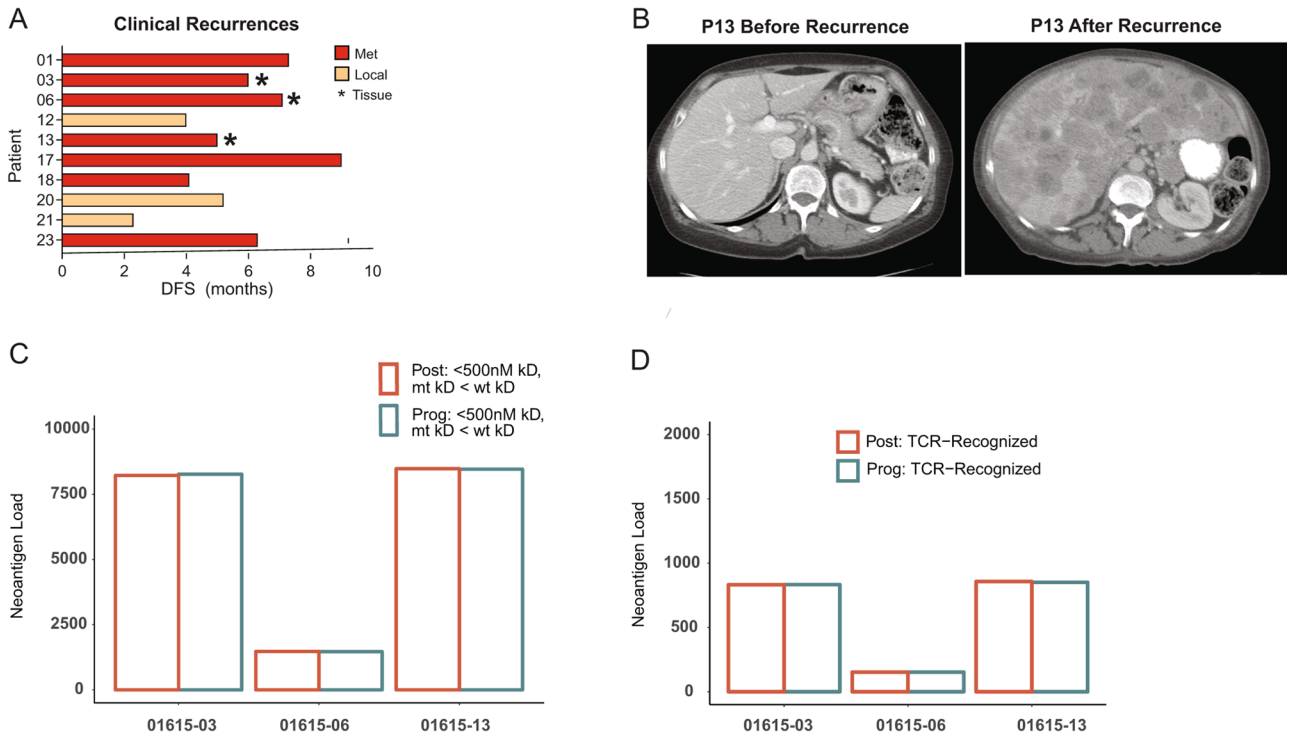

Extended Data Fig. 5 | Clinical progression and neoantigen quantity and quality. a, DFS of patients that recurred. **b**, CT image before and after of a patient with recurrent metastatic disease. **c**, Neoantigen load based on predicted binding (predicted k_D of < 500 nM and mutant k_D <wild-type k_D). **d**, Number of high-quality neoantigens that are likely to be recognized by TCRs based on neoantigen fitness model[42] at post-treatment versus recurrence time points.

nature research

Corresponding author(s): E. John Wherry, Tara Mitchell

Reporting Summary

Nature Research wishes to improve the reproducibility of the work that we publish. This form provides structure for consistency and transparency in reporting. For further information on Nature Research policies, see Authors & Referees and the Editorial Policy Checklist.

Statistical parameters

When statistical analyses are reported, confirm that the following items are present in the relevant location (e.g. figure legend, table legend, main text, or Methods section).

n/a	Confirmed	
☐	☒	The exact sample size (*n*) for each experimental group/condition, given as a discrete number and unit of measurement
☐	☒	An indication of whether measurements were taken from distinct samples or whether the same sample was measured repeatedly
☐	☒	The statistical test(s) used AND whether they are one- or two-sided *Only common tests should be described solely by name; describe more complex techniques in the Methods section.*
☐	☒	A description of all covariates tested
☐	☒	A description of any assumptions or corrections, such as tests of normality and adjustment for multiple comparisons
☐	☒	A full description of the statistics including central tendency (e.g. means) or other basic estimates (e.g. regression coefficient) AND variation (e.g. standard deviation) or associated estimates of uncertainty (e.g. confidence intervals)
☐	☒	For null hypothesis testing, the test statistic (e.g. *F*, *t*, *r*) with confidence intervals, effect sizes, degrees of freedom and *P* value noted *Give P values as exact values whenever suitable.*
☒	☐	For Bayesian analysis, information on the choice of priors and Markov chain Monte Carlo settings
☒	☐	For hierarchical and complex designs, identification of the appropriate level for tests and full reporting of outcomes
☐	☒	Estimates of effect sizes (e.g. Cohen's *d*, Pearson's *r*), indicating how they were calculated
☐	☒	Clearly defined error bars *State explicitly what error bars represent (e.g. SD, SE, CI)*

Our web collection on statistics for biologists may be useful.

Software and code

Policy information about availability of computer code

Data collection	Clinical trial data was collected using Penn's Clinical Trials Management System software called Velos eResearch. Flow cytometry data were collected on LSR II with FACSDiva software v8.0.1 (BD)
Data analysis	R package 'limma_3.34.9' was used to do pairwise comparisons of the normalized Nanostring gene expression data. R package 'pheatmap_1.0.10' was used for creating heatmaps to display Nanostring gene expression data. Metascape.org was used to enrich genes for GO biological processes. Gene set enrichment analysis (GSEA)(PMID:17644558) using Broad Institute software (https://software.broadinstitute.org/gsea/) was used to check for enrichment of gene signatures from microarray data in the Nanostring data. The GEP18 score was calculated as a weighted linear combination of 18 genes expression values for each sample. Statistical analyses were performed using either IBM SPSS v23 or Graphpad Prism v7. Flow cytometry analysis was performed using FlowJo v10

For manuscripts utilizing custom algorithms or software that are central to the research but not yet described in published literature, software must be made available to editors/reviewers upon request. We strongly encourage code deposition in a community repository (e.g. GitHub). See the Nature Research guidelines for submitting code & software for further information.

Data

Policy information about availability of data

All manuscripts must include a data availability statement. This statement should provide the following information, where applicable:

- Accession codes, unique identifiers, or web links for publicly available datasets
- A list of figures that have associated raw data
- A description of any restrictions on data availability

Nanostring data that support the findings have been deposited in NCBI Gene Expression Omnibus and are accessible through GEO Series accession number GSE123728. DNA whole exome sequencing data have been deposited in SRA and is accessible under SRA accession number PRJNA510621. All other relevant data are available from the corresponding author upon reasonable request.

Field-specific reporting

Please select the best fit for your research. If you are not sure, read the appropriate sections before making your selection.

☒ Life sciences ☐ Behavioural & social sciences ☐ Ecological, evolutionary & environmental sciences

For a reference copy of the document with all sections, see nature.com/authors/policies/ReportingSummary-flat.pdf

Life sciences study design

All studies must disclose on these points even when the disclosure is negative.

Sample size	As per the clinical protocol for UPCC 01615, Treatment of 30-32 patients will firmly establish the safety of the treatment (sAE of <33%). If the true underlying serious adverse rate is as low as 10%, then the failure to observe at least one adverse event in 32 treated patients, is <5% (binomial probability is 0.042). If the observed serious adverse event rate is 16.7% (5 of 30 patients), then the true event rate is likely to be no higher than 30% , since the upper bound of the 2-sided 95% confidence interval is 30%.
Data exclusions	None
Replication	Data including pathologic response, TIL infiltration, flow cytometry, and Nanostring gene expression has been successfully replicated with each patient sample considered a biologic replicate.
Randomization	This is Phase 1b clinical trial with no randomization. Subjects were enrolled by clearly defined inclusion and exclusion criteria with demographic data presented in Table 1. Predictive variables were controlled for covariates using univariable and multivariable analysis.
Blinding	All investigators and collaborators were blinded to clinical results when performing measurements and assays.

Reporting for specific materials, systems and methods

Materials & experimental systems

n/a	Involved in the study
☐	☒ Unique biological materials
☐	☒ Antibodies
☒	☐ Eukaryotic cell lines
☒	☐ Palaeontology
☒	☐ Animals and other organisms
☐	☒ Human research participants

Methods

n/a	Involved in the study
☒	☐ ChIP-seq
☐	☒ Flow cytometry
☒	☐ MRI-based neuroimaging

Unique biological materials

Policy information about availability of materials

Obtaining unique materials	Clinical trial samples from UPCC 01615 including blood and tumor samples are restricted and not available because of the limited amount of samples , most of which have already been used.

Antibodies

Antibodies used

Fresh trial PBMC and tumor suspension with stained with a master mix of antibodies for surface stains including CD4 (Biolegend Cat. 566355, OKT4,), CD8 (BD Cat. 564804, RPA-T8), CD45RA (Biolegend, HI100, 565702), Tim3 (Biolegend Cat. 345008, F38-2E2), Lag3 (ebioscience Cat. 48-2239-41, 3DS223H), CD39 (Biolegend Cat. 328206, A1), CD27 (BD Cat. 564302, L128), and PD-1 (BD Cat. 566112, EH-12) and intracellular stains for FoxP3 (BD Cat. 562421, 259D/C7), CTLA4 (BD Cat. 561717, BNI3), Eomes (ebioscience Cat. 61-4877-42, WD1928), Tbet (Biolegend Cat. 644824, 4B10), and Ki67 (BD Cat. 561277, B56).

Validation

Antibodies with high expression in the peripheral blood including CD4, CD8, CD45RA, CD27, PD-1, Eomes, Tbet, FoxP3, and CTLA-4 has been previously used, validated, and published (Huang et al, Nature 2017). We demonstrate high expression of Tim3, CD39, and Lag3 in the tumor and low expression in the blood as expected (Figure 3). Additional citation for these antibodies (Tim3, CD39, and Lag3) includes Thommen et al, Nature Medicine 2018 and our expression pattern is consistent with theirs.

Human research participants

Policy information about studies involving human research participants

Population characteristics

Patient Demographics are presented in Table1. Briefly, 59% of the patients had stage IIIC or IV disease (one patient with stage IV); the remainder of the patients had stage IIIB melanoma. 59% of the patients were male. 26% had an elevated LDH at baseline. One patient had received prior therapy (BRAF directed therapy).

Recruitment

This phase 1b clinical trial (NCT02434354), was a single institution investigator-initiated study sponsored by the University of Pennsylvania. The protocol and its amendments were approved by the Institutional Review Board at the University of Pennsylvania, and all patients provided written informed consent. Patients were eligible for enrolment if they were 18 years of age or older, had an Eastern Cooperative Group performance status of 0 or 1, adequate organ function according to protocol criteria, and had measurable resectable clinical stage III or resectable stage IV melanoma. Patients had to have an adequate tumor size, in the opinion of the surgical oncologist and study team, to allow for collection of biopsy tissue equivalent to at least two to four core biopsies for the pre-treatment biopsy, with an expectation that an equal or greater amount of tissue would remain after biopsy. Patients could not have received prior ipilimumab or other immune therapies. Prior BRAF directed therapies were permitted. Patients with uveal or mucosal melanoma were not eligible, nor were patients on systemic steroids or immunosuppression, patients who had received radiation to the resectable tumor, or patients with active brain metastasis. Patients seen at the University of Pennsylvania were recruited if they met eligibility criteria when seeing medical oncology or surgical oncology, including head and neck surgical oncology. Due to the fact that the primary sub-investigators were in surgical oncology, there may have been a bias leading to the inclusion of fewer patients with melanoma of the head and neck. However, the study did include patients with melanoma of the head and neck and we do not expect any impact on the study results.

Flow Cytometry

Plots

Confirm that:

☐ The axis labels state the marker and fluorochrome used (e.g. CD4-FITC).

☒ The axis scales are clearly visible. Include numbers along axes only for bottom left plot of group (a 'group' is an analysis of identical markers).

☒ All plots are contour plots with outliers or pseudocolor plots.

☒ A numerical value for number of cells or percentage (with statistics) is provided.

Methodology

Sample preparation

Methods: Sample Processing section

Instrument

LSR II

Software

Describe the software used to collect and analyze the flow cytometry data. For custom code that has been deposited into a community repository, provide accession details.

Cell population abundance

N/A

Gating strategy

Time Gate => FSC-A v SSC-A Lymphocyte Gate => FSC-A v FSC-H Singlet gate => CD3 v L/D and dump gate (Live CD3) = > CD4 v CD8

☐ Tick this box to confirm that a figure exemplifying the gating strategy is provided in the Supplementary Information.